A 0.5μA/Channel front-end for implantable and external ambulatory ECG recorders

Rezaeiyan, Yasser; Zamani, Milad; Shoaei, Omid; Serdijn, Wouter A.

DOI
10.1016/j.mejo.2018.01.016

Publication date
2018

Document Version
Accepted author manuscript

Published in
Microelectronics Journal

Microelectronics Journal

A 0.5 µA/Channel Front-End for Implantable and External Ambulatory ECG Recorders

Yasser Rezaeiyan[a], Milad Zamani[a], Omid Shoaei[a*], Wouter A. Serdijn[b]

[a]School of Electrical and Computer Engineering,University of Tehran, Tehran 1439957131, Iran
[b]Faculty of Electrical Engineering, Mathematics and Computer Science, Delft University of Technology, 2628 CD Delft, The Netherlands

ARTICLE INFO

Article history:

Keywords:
Analog integrated circuits
Bio-potential amplifier
Instrumentation amplifier
Low power
ECG
IECG
Programmable gain amp

ABSTRACT

There is an increasing demand for low power, low voltage, and small size analog readout bio-potential systems. This paper presents an analog front-end for measuring the intra-cardiac signals in implantable and also external ambulatory ECG cardiac recording applications. The analog front-end benefits from voltage to frequency conversion without conventional analog to digital conversion and thereby achieves a very low power consumption. The frequency averaging digital reconstruction makes an intrinsic low pass filter of which the cut-off frequency changes with the averaging interval and eliminates the need for an analog filter in this system. Furthermore, this feature enables the development of a general purpose analog readout bio-potential measurement system with programmable bandwidth. The proposed IC is fabricated in a 0.18 µm CMOS process and occupies 0.396 mm^2. It can measure intra-cardiac bio-potentials with 9.2-bit resolution while consuming just 0.5 µA per channel from a 1 V supply. The input referred noise of the intra-cardiac signal readout channel is 2 μV_{rms}.

1. INTRODUCTION

Cardiovascular diseases are among the leading causes of death. An abnormal rhythm of the heart is an early symptom of a heart disease and perhaps even heart failure, which can get worse if not treated. Monitoring the heart health condition continuously over long periods of time helps specialists to access a meaningful dataset to diagnose and cure this heart disease. Long term recording applications need a small device with a limited resource of power for ease of use. For example, a pacemaker is a disposable medical device that remains inside the body of patient for about 4 to 8 years before replacement by a new pacemaker with a fresh battery occurs [1]. Also, Implantable Loop Recorders (ILR) or External Event Recorders (EER) use ultra-low energy circuits and systems to record the signals over a long time [15].

A state-of-the-art recorder is required to sense the natural cardiac electric signals (either through peak detection or full waveform acquisition). As the sensing readout channel must continuously monitor the cardiac activity for a long time, the design of the front-end, often called the sense amplifier is very important and hence the design of the sense amplifier must be centered around ultra-low power consumption [2,3], [19].

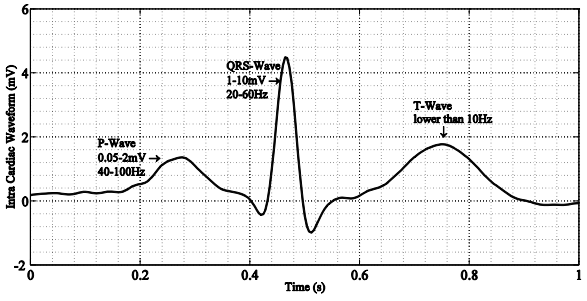

Fig. 1. Example of a human electrocardiogram.

* *Corresponding author.*
E-mail address: oshoaei@ut.ac.ir

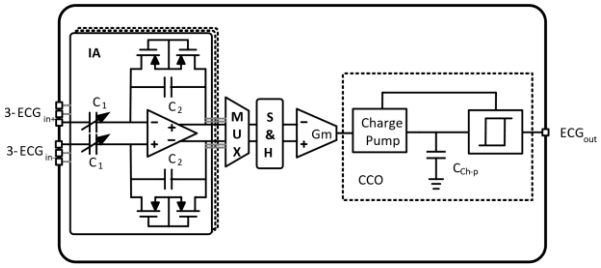

Fig. 2. Bio-potential measurement system architecture.

Fig. 1 shows an example of the intrinsic human heart waveform measured by means of external electrodes. The ventricular QRS signal occupies the 20-60 Hz frequency band with an amplitude range of 1-10 mV peak-to-peak. The atrial P signal occupies the 40-100 Hz frequency band with an amplitude range of 0.05-2 mV peak-to-peak. The T signal of ventricular repolarization contains frequencies below 10 Hz. The frequency range of disturbing bio-potential signals coming from muscles is from 100 Hz to 2 kHz and must be filtered out properly [1].

Conventional bio-potential measurement systems use an analog to digital converter to convert the amplified input signal into a digital format. High-gain amplifiers, various filters and high-resolution ADCs are among the usual building blocks of conventional bio-potential systems and consume large area and high power, which both are critical in wearable and implantable devices [4]-[11], [18]. The large amount of data generated by the ADC is then analyzed by a processor, stored and finally the modulated signal is transmitted for further processing. Digital signal processing, storage and transmission are power hungry processes [8].

In this paper, a novel analog front-end is proposed, the output of which is a PWM signal that can be directly processed by a digital processor and/or transmitted without full analog to digital conversion. The proposed system benefits from a voltage-to-frequency conversion technique [13] to produce a PWM signal, the frequency of which is directly related to the input voltage. Making use of a PWM output signal in an ADC-less system leads to reduction of the overall power consumption and area.

This paper is organized as follows: Section II describes the architecture of the proposed system that includes voltage to frequency conversion and presents its linearity analysis. Section III describes the circuit implementation and its specifications. Section IV presents the measurement results. Finally, Section V concludes the paper.

2. Architecture

The proposed bio-potential system uses a voltage to frequency conversion technique that is precise and simple to implement with minimum power consumption.

Fig. 2 shows the proposed system architecture with its constituting building blocks. The proposed system employs 3 instrumentation amplifiers (IA) as input blocks. The main core of the IA is an OTA with a high DC gain. The IA block benefits from capacitive feedback with intrinsic input offset cancelation. The input voltage of the system is a cardiac signal, which is in the range from very low voltages (of about 50 µV) to maxima of about 10 mV. As the dynamic range of the cardiac signal is large, the bio-potential system needs a programmable gain to adapt the dynamic range of the cardiac signal to the dynamic range of the subsequent blocks. The capacitive feedback provides gain programmability with three selectable

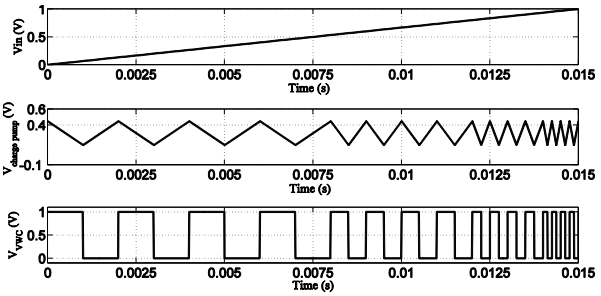

Fig. 3. Voltage-to-frequency concept. Using a ramp waveform as input voltage, the CCO capacitor voltage changes at a higher rate with higher input voltage. The output signal has a FSK-PWM waveform.

capacitances. The input referred noise of the IA is the dominant noise source of the whole system, since the first block with a high gain decreases the effect of the subsequent blocks on the input referred noise. The total noise of the IA is mainly due to the noise of the OTA. The negative feedback loop provides noise and signal filtering with a high-pass filter behavior.

The multiplexer selects one of the three IA output signals corresponding to three different leads that could sense three pacemaker, ILR or EER electrodes pairs. The sample-and-hold block holds the samples of the selected IA in each period for sensing. The differential output of the sample-and-hold is transformed into a current by means of a transconductance amplifier with a 1µS gain. The output current of the transconductor feeds the charge pump in the current-controlled oscillator (CCO) which produces a saw-tooth waveform by charging and discharging a capacitance via two controlling switches. These switches play a key role in controlling the time of charge and discharge. The value of the capacitance and the transconductor current determine the rate of this operation.

The next important block is a Schmitt trigger, which is responsible for comparing the saw-tooth waveform with the Schmitt trigger's high and low reference levels and changing its state accordingly. The Schmitt trigger is the most important block that affects the linearity of the whole system. The output of the Schmitt trigger provides the switching signals for the charge pump as well as the output of the bio-potential system. This output voltage is a pulse modulated signal that represents the bio-potential signal. A higher output pulse frequency means a higher cardiac input voltage that causes higher charging and discharging rate.

Fig. 3 shows an example of the generated signals and the concept of the used voltage to frequency conversion. The output current of the transconductor increases when the input voltage goes high. The higher output current of the transconductance increases the rate of charging and discharging. Consequently, the Schmitt trigger produces a higher PWM frequency from the saw-tooth voltage across the capacitance. Through counting the zero crossings of the pulses in a specific time interval, the input voltage of the cardiac signal can be reconstructed from the output PWM voltage as will be explained next.

2.1. Voltage to Frequency Transfer Function

The output period, T, is the duration of subsequent charging (T_{ch}) and discharging (T_{disch}) within the Schmitt trigger decision levels. It holds:

$$f = \frac{1}{T_{ch} + T_{disch}} = \frac{1}{T}. \quad (1)$$

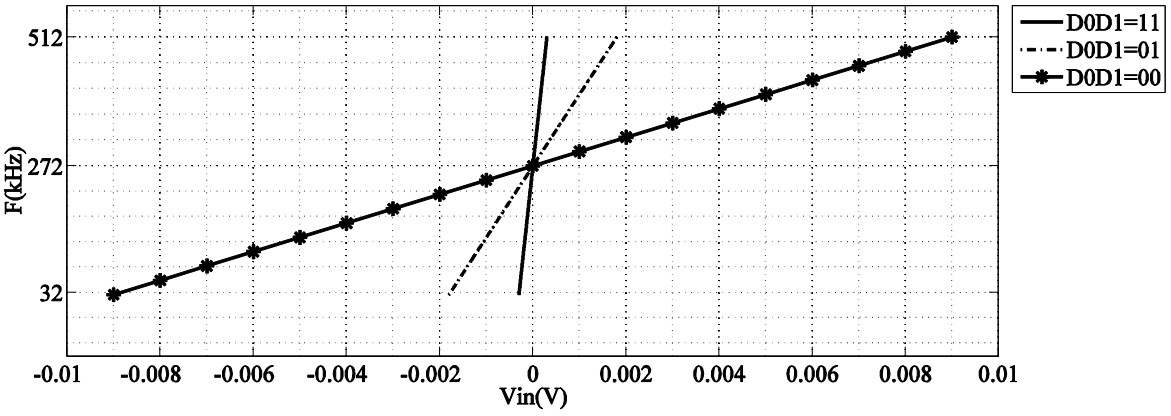

Fig. 4. Transfer function of the bio-potential system.

Supposing the same amount of charge and discharge current, the charging and discharging times are equal, and the period of the output PWM can be written as:

$$T = T_{ch} + T_{disch} = \frac{2C_{ch.p}V_{Hys}}{I}, \tag{2}$$

where I is the current of the charge pump, $C_{ch.p}$ is the capacitance of the charge pump and V_{Hys} is the hysteresis voltage of the Schmitt trigger. The momentary frequency of the output PWM signal can be written as:

$$f_{out}(t) = f_0 + \frac{A_{IA}G_m}{2C_{ch.p}V_{Hys}}V_{in}(t), \tag{3}$$

where A_{IA} is the gain of the input instrumentation amplifier and G_m is the gain of the transconductor. f_0 is the mean frequency of the output PWM signal which is related to the dc current of the G_m and allows for reading in also negative cardiac input voltages.

The output frequency is inversely proportional to the charge-pump capacitance and hysteresis voltage. In addition, the programmable gain of the input IA changes the frequency directly. Thus, the IA plays a key role in increasing the dynamic range and also determines the frequency range, simultaneously.

The input voltage data lies in the output PWM frequency which can be written as [14]:

$$y(t) = \frac{1}{2} + \frac{2}{\pi}\sum_{k=1}^{\infty}\frac{1}{k}\sin(\frac{k\pi}{2})\cos(2k\pi f_{out}t). \tag{4}$$

The reconstruction of the input signal from the output PWM is done by counting the zero-crossings of the output PWM signal in a specific time interval and then using (4).

Fig. 4 shows the transfer function of the bio-potential channel. To maximize the readout dynamic range, 3 different gain settings are utilized to change the slope of the output frequency according to Equation 3. The minimum output frequency of each region is bound to 32 kHz to have minimally a 6-bit representation of the input signal counting both positive and negative edges in a 1 ms sampling interval. The maximum output frequency of each region is bound to 512 kHz to prevent excessive dynamic power consumption and to limit the effect of jitter.

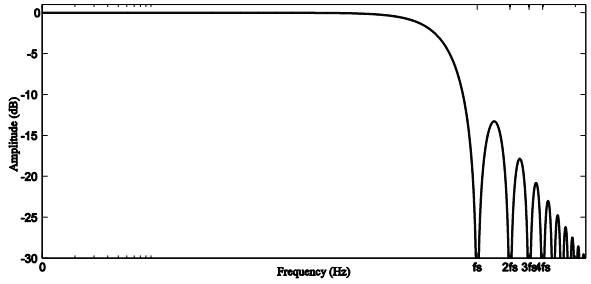

Fig. 5. Frequency response of the moving average filtering concept.

The reconstruction procedure is the averaging of the frequency in each interval. This makes the reconstruction transfer function a low pass filter. The number of zero crossings of the output PWM signal is related to the mean frequency in a specific interval and also the mean of the input cardiac signal in that interval.

$$N_{Zerocross} \propto \overline{F_{out}} \propto \overline{V_{in}}. \tag{5}$$

The reconstructed Y_{out} is the average of the input voltage in a mean interval time (T_S):

$$Y_{out}(T_s, t) = \frac{k}{T_s}\int_{t-T_s}^{t} V_{in}(\tau)d\tau, \tag{6}$$

where k is a scaling coefficient.

The output transfer function of this averaging operation can be written as:

$$h(t) = \frac{k}{T_s}\int_{t-T_s}^{t}\delta(\tau)d\tau = \frac{k}{T_s}\left[u(t) - u(t-T_s)\right] \tag{7}$$

and in the frequency domain as:

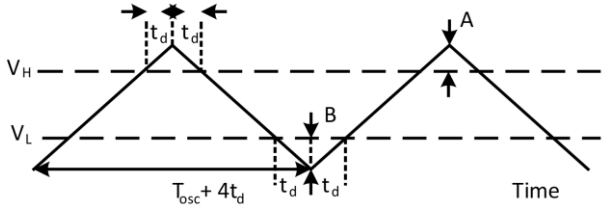

Fig. 6. The level detector delay as the major cause of non-linearity.

$$H(j\omega) = \frac{2k\sin(\frac{T_s\omega}{2})}{\omega T_s}. \quad (8)$$

This frequency-domain transfer function reveals that the averaging provides a low-pass filter function of which the cut-off frequency changes with the averaging interval (Fig. 5).

Nonlinearity can affect the output frequency of the bio-potential channel. In the following sections, the effect of nonlinearity on the output frequency are explained and closed-form expressions are extracted. These expressions allow the selection of appropriate circuit parameters that are used for optimization.

2.2. Linearity Analysis

The linearity of the bio-potential measurement system is very important since the reconstruction after removing the DC value is based on the linear relation of input voltage and output frequency. The output frequency is:

$$f_{out} = \frac{A_{IA}G_m}{2C_{ch.p}V_{Hys}}V_{in}(t) = A_{vf}V_{in}(t). \quad (9)$$

Fig. 6 shows the most important cause of non-linearity in the voltage to frequency conversion, being the delay in the decision making process in the Schmitt trigger, which creates an error in the hysteresis voltage, according to:

$$f_{out} = \frac{I}{2C_{ch.p}(V_{Hys}+V_{error})} = f_{osc}\times\frac{1}{1+\frac{V_{error}}{V_{Hys}}}, \quad (10)$$

where

$$V_{error} = A+B = \frac{2I}{C_{ch.p}}\times t_d = 4V_{Hys}f_{osc}t_d, \quad (11)$$

where t_d is the delay of the charge-pump supposing that the delay of the rise time and fall time are the same for the sake of simplicity. We can calculate the oscillation frequency using a Taylor series as:

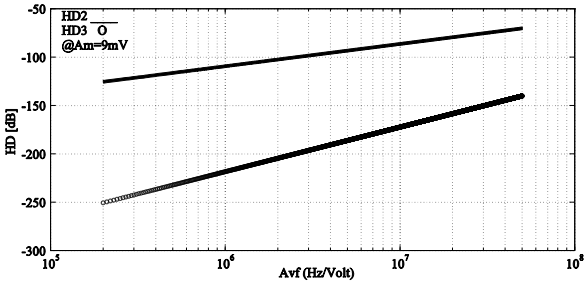

Fig.7. The second and third harmonic distortion of the system versus the front-end gain.

$$f_{out} = f_{osc}\times\sum_{n=0}^{\infty}(-1)^n(\frac{V_{error}}{V_{Hys}})^n. \quad (12)$$

In order to estimate the harmonic distortion in f_{out}, using (12), we can calculate:

$$f_{out} = f_{osc} - 4f_{osc}^2t_d + 16f_{osc}^3t_d^2 - 64f_{osc}^4t_d^3. \quad (13)$$

Combining (9) and (13) we obtain:

$$f_{out} = A_{vf}V_{in} - 4t_dA_{vf}^2V_{in}^2 + 16t_d^2A_{vf}^3V_{in}^3 - 64t_d^3A_{vf}^4V_{in}^4. \quad (14)$$

Equation (14) shows the output frequency as a function of the input voltage. From this, the second and third order harmonic distortions are calculated as:

$$HD_2 = \left|\frac{32t_d^3A_{vf}^4A_m^4 - 2t_dA_{vf}^2A_m^2}{A_{vf}A_m + 12t_d^2A_{vf}^3A_m^3}\right| \quad (15)$$

$$HD_3 = \left|\frac{4t_d^2A_{vf}^3A_m^3}{A_{vf}A_m + 12t_d^2A_{vf}^3A_m^3}\right|. \quad (16)$$

where t_d, A_{vf}, and A_m are the Schmitt-trigger delay, the front-end gain and the amplitude of the input signal, respectively.

When the second and third harmonic distortion components increase this deteriorates the system linearity. Fig. 7 shows the 2nd- and 3rd-order harmonic distortions of the front-end for a large sinusoidal input signal amplitude (A_m=9 mV) and for the lowest front-end gain. For a second harmonic value lower than -70 dB, the front-end gain must be lower than 30 MHz/V, so the gain is set with a more than 10% margin (26.6 MHz/V). The same approach is utilized to define also the other gain settings.

The Schmitt-trigger delay is the most important factor that affects the harmonic distortion and the linearity of the system according to (15) and (16). Moreover, with the minimum possible front-end gain the system shows maximum linearity.

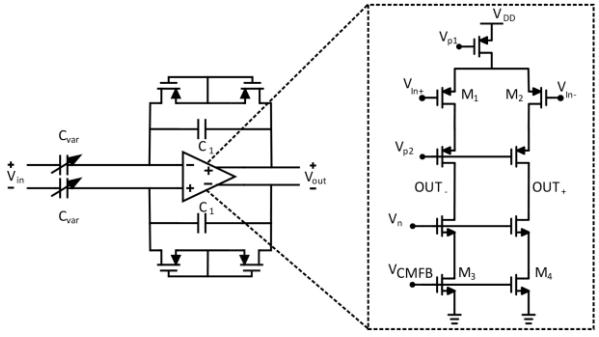

Fig. 8. Block diagram of the IA. The core block of the IA is an OTA with a telescopic cascode.

3. Circuit Implementation

Fig. 8 shows the circuit diagram of the input instrumentation amplifier of the proposed system. The DC offset from the lead is rejected by the AC-coupled band-pass filter configuration. The high-pass cut-off frequency is set by the pseudo resistor transistors and feedback capacitances C_1 according to:

$$f_{cut-off} = \frac{1}{2\pi R_{pseudoR} C_1}, \tag{17}$$

where $R_{pseudoR}$ is the pseudo resistance of two transistors in anti-series. The required cut-off frequency is 10 Hz and so the pseudo resistance value should be larger than 100 MΩ. To guarantee that the high-pass cutoff frequency is sufficiently low, medium-voltage pMOS transistors were adopted. Moreover, the pseudo resistance value variation is low and stable due to the low swing of the IA's output voltage.

The IA has three different gain settings to increase the input dynamic range, which are set by the ratio of the input capacitance C_{var} and feedback capacitance C_1. The high-pass cut-off frequency is about 2 Hz which is low enough for the band of interest of the ECG signal.

The noise of the pseudo resistors and the OTA affects the IA input referred noise. Due to the wide bandwidth, the OTA is the dominant noise source of the IA. It is a common telescopic cascode amplifier. The input referred noise of the IA can be written as:

$$\overline{V_{in,IA}^2} = \overline{V_{in,OTA}^2} \cdot (1 + \frac{C_1}{C_{\text{var}}})^2 \tag{18}$$

where $V_{in,OTA}^2$ is the input referred noise of the OTA, which can be expressed as:

$$\overline{V_{IN,OTA}^2} = \frac{8KT}{g_{m1,2}}(\gamma_{1,2} + \frac{\gamma_{3,4} g_{m3,4}}{g_{m1,2}}) + \frac{2k_p}{(WL)_{1,2} C_{ox} f} + \frac{2k_n}{(WL)_{3,4} C_{ox} f} \times \frac{g_{m3,4}^2}{g_{m1,2}^2}, \tag{19}$$

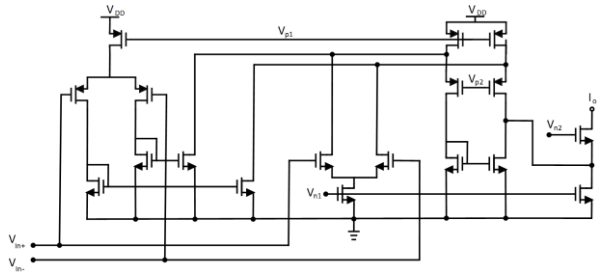

Fig. 9. Transconductor architecture: a rail-to-rail input folded cascode.

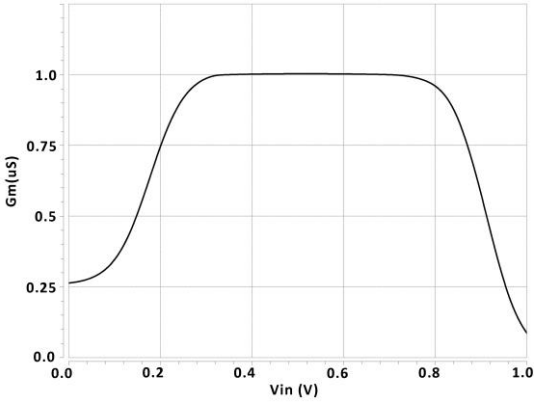

Fig. 10. Simulated transconductance behavior versus common mode input voltage.

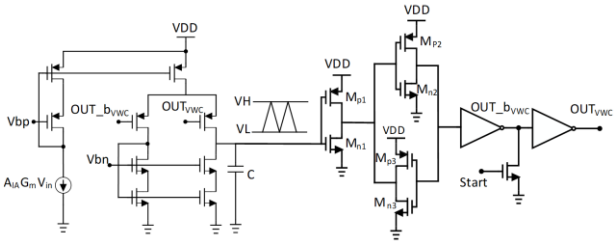

Fig. 11. Voltage-to-frequency convertor: a charge pump, a Schmitt trigger and two inverters.

where k_n, k_p, C_{ox}, $\gamma_{n,m}$, g_m, $W_{n,m}$ and $L_{n,m}$ denote the *1/f* noise coefficients of NMOS and PMOS devices, the gate oxide capacitance per unit area, thermal noise coefficients, transconductance of devices, the width and the length of transistors, respectively, the transistor number of which have been specified in Fig. 8.

Fig. 9 shows the transconductance amplifier that produces the required current to the charge pump: a folded cascode amplifier designed with both PMOS and NMOS input pairs with minimum stack transistors [7]. The non-linearity of the transconductance amplifier directly affects the system non-linearity. Using a rail-to-rail input stage, the linearity of voltage-to-current converter is guaranteed even under low supply voltage. Fig. 10 shows the simulated g_m of the transconductance amplifier, which is linear across the operational input voltage swing. The maximum input voltage swing of the transconductance amplifier is 120 $mV_{p\text{-}p}$.

Fig. 11 shows the overall circuit of the voltage-to-frequency converter (VFC). The VFC consists of a charge pump and a Schmitt trigger. The charge pump mirrors the output current of the transconductance amplifier and provides a sink and source path with an NMOS and a PMOS transistor,

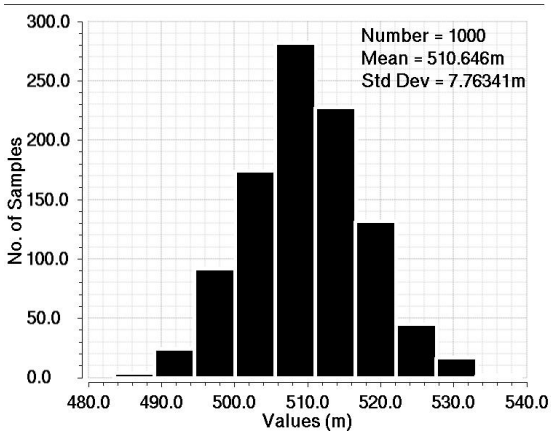

Fig. 12. Monte-Carlo simulation of the Schmitt trigger hysteresis voltage.

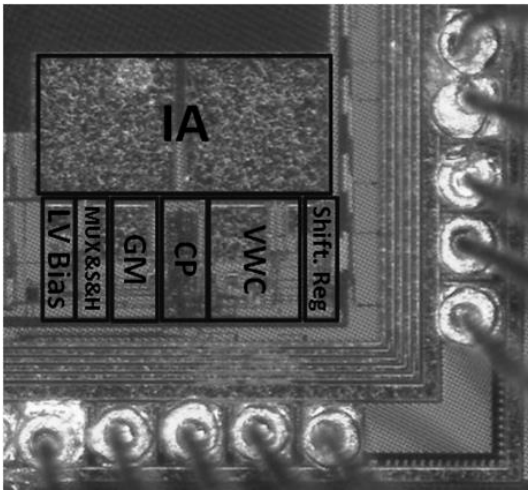

Fig. 13. Chip micrograph.

respectively. The input voltages that cause the output to change from 0 to 1 and from 1 to 0 can be written as (20) and (21), where $V_{INV\text{-}IH}$ and $V_{INV\text{-}IL}$ are the high and low levels of the inverter where the gain is -1, respectively. Fig. 12 shows the result of a Monte-Carlo simulation of the hysteresis voltage, which confirms the low sensitivity to process variations. As the level detector benefits from two back-to-back inverters with positive feedback, the transition of the output voltage is with minimum delay. This positive feedback guarantees a minimum delay and thereby minimum

TABLE I
DESIGN SPECIFICATION AND MEASUREMENT SUMMARY

	Target Specification	Measurement Result
Operating voltage	1 V	1 V
Gain	14-28-44 dB	14-28.5-44 dB
BW	10 – 120 Hz	8 – 120 Hz
Input Dynamic Range	±50 µVpp/ ±10 mVpp	±50 µVpp/ ±9 mVpp
CMRR	>90 dB	>90 dB
Input Referred Noise	< 5 µVpp Over 150 Hz	2 μV_{rms}
Output Freq. Range	Up to 512 kHz	Up to 512 kHz
Power Consumption per channel	< 0.5 µW	0.5 µW

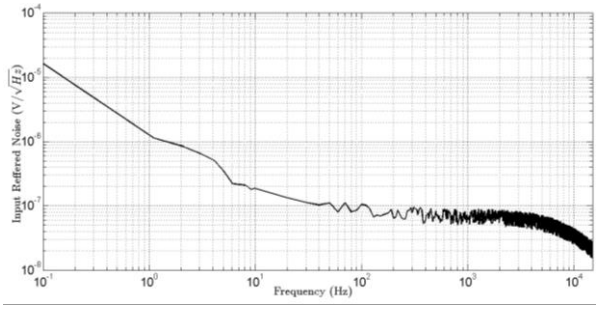

Fig. 14. Measured bio-potential channel input referred noise (the gain is 44 dB and C_{var} value is 80pF).

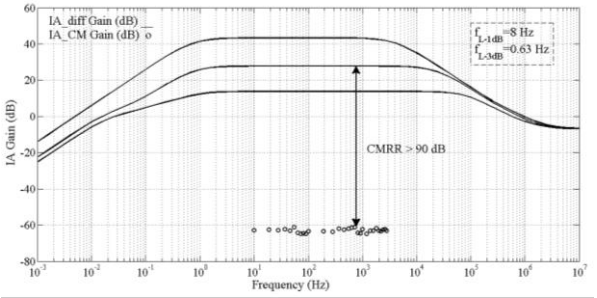

Fig. 15. Measured transfer function of the IA and its filtering characteristic.

hysteresis change for a corresponding input frequency range. The output current of the charge pump charges and discharges capacitor *C* shown in Fig. 11 and produces a triangular waveform. The starting signal acts as a trigger signal of the VFC and sets the initial condition.

$$V_{Hyst-LH} = \frac{\sqrt{\mu_p (V_{DD} - V_{Inv-IH}) \left[\mu_p \left(\frac{w}{l}\right)^2_{p1} (V_{DD} - V_{Inv-IH}) + 2\mu_n \left(\frac{w}{l}\right)_{n1} (V_{DD} - |V_{THp}|) \left(\left(\frac{w}{l}\right)_{p1} + \left(\frac{w}{l}\right)_{p2} \right) + 2 \left(\frac{w}{l}\right)_{n1} \left(\frac{w}{l}\right)_{p1} \mu_n |V_{THp}| \right]} + \left(\frac{w}{l}\right)_{p1} \mu_p (V_{Inv-IH} - V_{DD}) + \left(\frac{w}{l}\right)_{n1} \mu_n |V_{THp}|}{\left(\frac{w}{l}\right)_{p1} \mu_p} \quad (20)$$

$$V_{Hyst-HL} = \frac{\sqrt{\mu_n V_{Inv-IL} \left[\mu_n \left(\frac{w}{l}\right)^2_{n1} V_{Inv-IL} + 2\mu_p \left(\frac{w}{l}\right)_{p1} (V_{DD} - V_{THn}) \left[\left(\frac{w}{l}\right)_{n1} + \left(\frac{w}{l}\right)_{n2} \right] - 2 \left(\frac{w}{l}\right)_{p1} \left(\frac{w}{l}\right)_{n1} \mu_p |V_{THp}| \right]} + \left(\frac{w}{l}\right)_{p1} \mu_p (V_{DD} - |V_{THp}|) + \left(\frac{w}{l}\right)_{n1} \mu_n V_{Inv-IL}}{\left(\frac{w}{l}\right)_{p1} \mu_p} \quad (21)$$

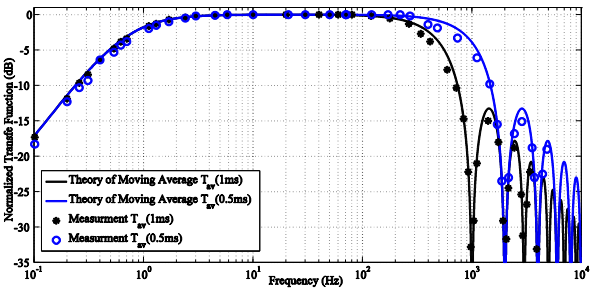

Fig. 16. Comparison of theoretical averaging function and measurements for two different averaging intervals (0.5 ms and 1 ms).

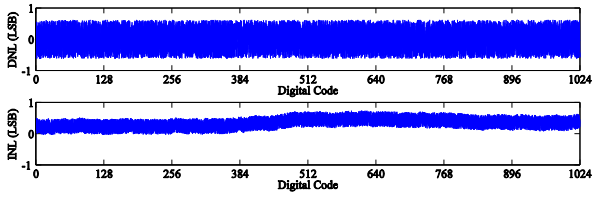

Fig. 17. Measured DNL and INL performance.

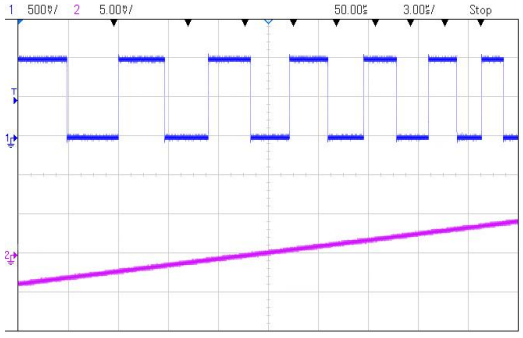

Fig. 18. Example of a measured output signal of the proposed system for a ramp input signal (A_{IA}=14 dB).

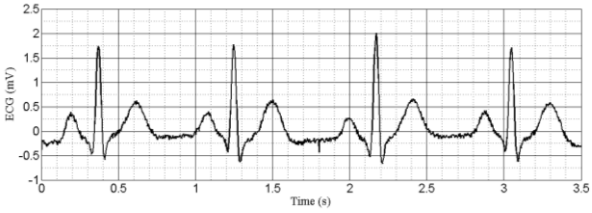

Fig. 19. Example of a measured bio-potential signal of a human ECG stored in a signal generator, after reconstruction.

TABLE II
BIO-POTENTIAL PERFORMANCE SUMMARY AND COMPARISON WITH THE STATE OF THE ART

	This Work	[12]	[9]	[3]	[5]	[7]	[16]	[18]
Technology (µm)	0.18	0.18	0.5	0.18	0.35	0.18	0.13	0.18
Supply voltage (V)	1	1.25	2	2.2	1	1	0.3	0.5
Type of sensor	IECG	ECG	ECG	IECG	ECG	ECG	ECG	ECG
Number of channels	3	1	1	3	1	1	1	1
resolution (ENOB)	9.2	8	10.6	9.4	10.2	8	4.4	9.39
input referred noise (μV_{rms}) (50 mHz-150 Hz)	2	16.8	1.1	2.2	2.5	3.77	n.a.	2.8 (0.5-250 Hz)
CMRR (dB)	90	n.a.	105	100	71.2	67	n.a.	106
PSRR (dB)	71	n.a.	n.a.	93	84	n.a.	n.a.	73
Overall system size (mm × mm)	0.63 × 0.63	1.9 × 2	5 × 5	3.5 × 1.4	1 × 1	0.71 × 0.69	0.42 × 0.85	1 × 1
Power consumption (µW) per channel	0.5	9.7	9.4	2.46	0.895	8.49	0.22	0.6

The proposed bio-potential system also produces an output signal that is suitable for very low power transmission via backscattering [17]. Backscattering is also good from a security perspective, as repeated attacks/requests will not drain the battery. The modulation is done via switching circuitry by means of on-off keying (OOK) or load-shift keying at 13.56 MHz.

4. Measurement results

The proposed bio-potential measurement system has been fabricated in a 0.18 µm CMOS process and occupies 0.396 mm^2. Fig. 13 shows the chip micrograph. Table I shows the design specifications and measurement summary of the system.

The input referred noise of the IECG/ECG readout channel measured over a signal bandwidth of 50 mHz-150 Hz is 2 μV_{rms}, as shown in Fig. 14, for each channel. Fig. 15 shows the transfer function of the IA and its filtering characteristic for three different gain settings. The CMRR of the IA is higher than 90 dB. Fig. 16 shows the comparison of the measurement and theoretical averaging function with two different averaging intervals (0.5 ms and 1 ms), which provides a low-pass filter function of which the averaging interval changes the cut-off frequency.

The result after the reconstruction of the proposed system is similar to that of an analog to digital converter. The frequency of the multiplexer is set to 1 kHz and 3 kHz; the system effective number of bits is 9.2bits and 8.4bits, respectively. Making use of the same parameters defined for ADC's we can extract the DNL and INL of the proposed system. Fig 17 shows the DNL and INL characterization. A ramp input signal with increasing voltage causes the frequency to increase. Fig. 18 shows the output of the proposed system for a ramp input signal. The reconstructed bio-potential signal of a human ECG stored in a signal generator is shown in Fig. 19 to illustrate the

functionality of the proposed system. Table II shows the comparison of the proposed system with a few state-of-the-art designs. Among these works, the proposed system features the lowest required supply voltage and also the lowest power consumption with only 500 nA for each channel.

5. Conclusion

A 0.5 µA/channel bio-potential measurement technique and IC is presented for measuring cardiac signals making use of a voltage to frequency converter that enables very low power operation. The frequency averaging of the reconstruction procedure makes an intrinsic low pass filter transfer function. The proposed system consists of three independent channels with 9.2-bit resolution.

REFERENCES

[1] J. G. Webster, Design of Cardiac Pacemaker. Piscataway, NJ, USA: IEEE Press, 1995.

[2] L. Lentola, A. Mozzi, A. Neviani and A. Baschirotto, "A 1-µA front end for pacemaker atrial sensing channels with early sensing capability," in IEEE Transactions on Circuits and Systems II: Analog and Digital Signal Processing, vol. 50, no. 8, pp. 397-403, Aug. 2003.

[3] L. Yan et al., "A 13µ Analog Signal Processing IC for Accurate Recognition of Multiple Intra-Cardiac Signals," in IEEE Transactions on Biomedical Circuits and Systems, vol. 7, no. 6, pp. 785-795, Dec. 2013.

[4] A. Gerosa, A. Maniero and A. Neviani, "A fully integrated dual-channel log-domain programmable preamplifier and filter for an implantable cardiac pacemaker," in IEEE Transactions on Circuits and Systems I: Regular Papers, vol. 51, no. 10, pp. 1916-1925, Oct. 2004.

[5] X. Zou, X. Xu, L. Yao and Y. Lian, "A 1-V 450-nW Fully Integrated Programmable Biomedical Sensor Interface Chip," in IEEE Journal of Solid-State Circuits, vol. 44, no. 4, pp. 1067-1077, April 2009.

[6] H. Kim et al., "A Configurable and Low-Power Mixed Signal SoC for Portable ECG Monitoring Applications," inIEEE Transactions on Biomedical Circuits and Systems, vol. 8, no. 2, pp. 257-267, April 2014.

[7] Y. Li, A. L. Mansano, Y. Yuan, D. Zhao and W. A. Serdijn, "An ECG Recording Front-End With Continuous-Time Level-Crossing Sampling," in IEEE Transactions on Biomedical Circuits and Systems, vol. 8, no. 5, pp. 626-635, Oct. 2014.

[8] S. Y. Lee et al., "A Programmable Implantable Microstimulator SoC With Wireless Telemetry: Application in Closed-Loop Endocardial Stimulation for Cardiac Pacemaker," in IEEE Transactions on Biomedical Circuits and Systems, vol. 5, no. 6, pp. 511-522, Dec. 2011.

[9] R. F. Yazicioglu, S. Kim, T. Torfs, H. Kim and C. Van Hoof, "A 30 µW Analog Signal Processor ASIC for Portable Biopotential Signal Monitoring," in IEEE Journal of Solid-State Circuits, vol. 46, no. 1, pp. 209-223, Jan. 2011.

[10] L. S. Y. Wong, S. Hossain, A. Ta, J. Edvinsson, D. H. Rivas and H. Naas, "A very low-power CMOS mixed-signal IC for implantable pacemaker applications," in IEEE Journal of Solid-State Circuits, vol. 39, no. 12, pp. 2446-2456, Dec. 2004.

[11] L. Yan et al., "A 680 nA ECG Acquisition IC for Leadless Pacemaker Applications," in IEEE Transactions on Biomedical Circuits and Systems, vol. 8, no. 6, pp. 779-786, Dec. 2014.

[12] A. L. Mansano, Y. Li, S. Bagga and W. A. Serdijn, "An Autonomous Wireless Sensor Node With Asynchronous ECG Monitoring in 0.18 µm CMOS," in IEEE Transactions on Biomedical Circuits and Systems, vol. 10, no. 3, pp. 602-611, June 2016.

[13] P. M. Nadeau, A. Paidimarri and A. P. Chandrakasan, "Ultra Low-Energy Relaxation Oscillator With 230 fJ/cycle Efficiency," in IEEE Journal of Solid-State Circuits, vol. 51, no. 4, pp. 789-799, April 2016.

[14] R. A. Guinee and C. Lyden, "A novel Fourier series time function for modeling and simulation of PWM," in IEEE Transactions on Circuits and Systems I: Regular Papers, vol. 52, no. 11, pp. 2427-2435, Nov. 2005.

[15] O. Andersson, K. H. Chon, L. Sörnmo and J. N. Rodrigues, "A 290 mV Sub- $V_{\rm T}$ ASIC for Real-Time Atrial Fibrillation Detection," in IEEE Transactions on Biomedical Circuits and Systems, vol. 9, no. 3, pp. 377-386, June 2015.

[16] X. Zhang and Y. Lian, "A 300-mV 220-nW Event-Driven ADC With Real-Time QRS Detection for Wearable ECG Sensors," in IEEE Transactions on Biomedical Circuits and Systems, vol. 8, no. 6, pp. 834-843, Dec. 2014.

[17] A. Shameli, A. Safarian, A. Rofougaran, M. Rofougaran, J. Castaneda and F. De Flaviis, "A UHF Near-Field RFID System With Fully Integrated Transponder," in *IEEE Transactions on Microwave Theory and Techniques*, vol. 56, no. 5, pp. 1267-1277, May 2008.

[18] Z. Zhu and W. Bai, "A 0.5-V 1.3- µW Analog Front-End CMOS Circuit," in *IEEE Transactions on Circuits and Systems II: Express Briefs*, vol. 63, no. 6, pp. 523-527, June 2016.

[19] Wenbin Bai, Zhangming Zhu, “A 0.5-V power-efficient low-noise CMOS instrumentation amplifier for wireless biosensor,” in Microelectronics Journal, vol. 51, pp 30-37, May 2016.